Draft version August 22, 2025
Typeset using LaTeX **preprint** style in AASTeX631

Ab Initio Entropy Calculations of Water Predict the Interiors of Uranus and Neptune to be 15–30% Colder than Previous Models

Burkhard Militzer[1]

[1]*Department of Earth and Planetary Science, Department of Astronomy, University of California, Berkeley, CA, 94720, USA*

ABSTRACT

Ab initio free energy calculations are employed to derive the entropy of liquid and superionic water over a wide range of conditions in the interiors of Uranus and Neptune. The resulting adiabats are much shallower in pressure-temperature space than those adopted for earlier models of Uranus and Neptune. Our models for their interiors are thus much colder, increasing the likelihood that diamond rain or the recently predicted phase separation of planetary ices has occurred in the mantles of ice giant planets. Based on our *ab initio* data, we construct interior models for Uranus and Neptune with the Concentric MacLaurin Spheroid method that match the existing gravity measurements. We compare fully convective models with models that include a convective boundary between liquid and superionic water. We also share a code to characterize giant planet atmospheres where para and ortho hydrogen as well as helium are present.

1. INTRODUCTION

The primary mechanism for secular cooling within planets is convection because heat transport via diffusion and radiation is comparatively inefficient (Hubbard 1984). The magnetic fields of Jupiter, Saturn, Uranus and Neptune but also that of Earth and Mercury provide direct evidence that convection occurs in their interiors. Ample evidence of plate tectonics in our plant demonstrates that convection also occurs in solid, highly viscous layers. For Uranus and Neptune this implies that if there existed a layer of superionic water in their interior, it would mostly likely be convective (Matusalem et al. 2022). For convection not to occur either requires an endothermic first order phase transition (Schubert et al. 1975) or the presence of a gradient in composition (Leconte & Chabrier 2012). If a planet's interior has differentiated into multiple convective layers the most plausible assumption would be to represent each layer by an adiabat and to match pressure and temperature at the boundaries (Hubbard 1984). The entropy of the outermost layer can typically be constrained by observations.

NASA has made a Uranus orbiter and probe mission a priority for this decade (NASA 2021) generating new interest in understanding the formation and interior structure of Uranus and Neptune. Comparatively little is known about these two ice giant planets because so far they have only been visited by only a single spacecraft, Voyager 2, which during its fly-bys in 1986 and 1989 made the surprising discovery that both planets have nondipolar magnetic fields. Ruzmaikin & Starchenko (1991) and Stanley & Bloxham (2004, 2006) showed that such fields emerge if they are generated from convection restricted to a thin outer mantle layer. Consistent with that interpretation, Militzer

(2024a) proposed the outer layer is composed of water and hydrogen while there is an inner layer composed of carbon, nitrogen and a depth dependent concentration of hydrogen, which stabilizes this layer against convection. This structure was based on the spontaneous phase separation of planetary ices that was observed in *ab initio* simulations of H_2O, CH_4, and NH_3 at high pressure and temperature. The resulting models were consistent with the gravity measurements and the proposed geometry for the magnetic dynamo layer.

As an alternative explanation for the nondipolar fields, Soderlund et al. (2013) performed magneto-hydrodynamic simulations of Uranus's and Neptune's magnetic fields assuming thick and thin shell dynamos. They suggested that the nondipolar magnetic fields are the result of turbulent convection that is driven by thermal buoyancy. Various dynamo types are discussed by Soderlund & Stanley (2020).

The interpretation of the gravity measurements has not been unique (Movshovitz & Fortney 2022) but it is generally assumed that a large part of their interior is composed of planetary ices, H_2O, CH_4, and NH_3 (Podolak et al. 1995). Helled et al. (2020) reviewed the different methods and assumptions that have been invoked to characterize the structure and evolution of Uranus and Neptune. Nettelmann et al. (2013) matched the available gravity data with interior models consisting of three layers, each homogeneous and convective. The outer two layers are composed of hydrogen, helium, and water, though their compositions differ, while the innermost layer is a rocky core.

Helled & Bodenheimer (2014) developed core-accretion models for Uranus and Neptune, investigating the conditions that resulted in the observed masses and solid-to-gas ratios. Bailey & Stevenson (2021) suggested that the difference in heat flux between Uranus and Neptune indicates varying levels of water-hydrogen mixing in their outer envelopes. Movshovitz & Fortney (2022) constructed ensembles of interior models for Uranus and Neptune with agnostic pressure-density relationships, constrained their moments of inertia and discussed gravity measurements of a future low-periapse orbiter.

Neuenschwander et al. (2024) investigated the possible relationships of pressure, density, temperature and composition by incorporating convective and nonconvective layers into Uranus's interior and compared models that include a water-rich layer with those that do not. Most recently Lin et al. (2025) constructed interior models for Uranus under a variety of assumptions and concluded that its mantle cannot be composed solely of water. French et al. (2024) provided additional constraints for Uranus's gravity coefficients by analyzing occultation data for its rings. Stixrude et al. (2021) investigated the thermal evolution of Uranus's interior and proposed that the lack of a strong heat flux might be due to the formation of a growing core composed of superionic water.

The relevance of superionic water to planetary science was first demonstrated by Cavazzoni et al. (1999) who showed with *ab initio* computer simulations that at high pressure and elevated temperatures, water assumes a hydrid state, in which the larger oxygen atoms remain confined to their lattice sites like atoms in a solid while the smaller hydrogen nuclei diffuse through the oxygen sublattice like the atoms of a liquid. French et al. (2009) and Redmer et al. (2011) performed simulations of a wider range of pressure-temperature conditions and predicted superionic water to exist in the interiors of Uranus and Neptune. At that point, all simulations of superionic water had assumed a body-centered cubic (bcc) lattice at oxygen atoms because Cavazzoni et al. (1999) had initialized their simulations with solid ice X structure. Wilson et al. (2013) demonstrated with *ab initio* Gibbs free energy calculations that a more densely packed face-centered cubic (fcc) structure is thermodynamically preferred

for most pressure-temperature conditions. With novel shock compression experiments, Millot et al. (2019) confirmed the existence of the superionic fcc phase. Later diamond anvil cell experiments by Prakapenka et al. (2021) showed that the bcc structure exists but it is confined to a rather small range of pressure-temperature conditions and probably not relevant for ice giant interiors as we illustrate in Fig. 1. Superionic behavior has also been predicted in H_2O-NH_3 mixtures (Bethkenhagen et al. 2015) and will likely be a very common phenomenon among OCNH compounds (de Villa et al. 2023, 2025). At ∼20 Mbar, superionic fcc structure has been predicted to transform into a different superionic structure with $P2_1/c$ symmetry (Sun et al. 2015; Militzer & Zhang 2018) but the required pressures exceed the conditions in the interiors of Uranus and Neptune.

In this paper, we report results from *ab initio* computer simulations of liquid and fcc superionic water under conditions of ice giant interiors. As we explain in the following Methods section, we first describe how we calculate adiabats of mixtures of para and ortho hydrogen with helium in the atmospheres of Uranus and Neptune, which enables us to derive adiabats for their atmospheres. Then we describe our *ab initio* simulations and thermodynamic integration (TDI) method to derive the entropy as a function of density and temperature, which allows us to construct adiabatic temperature profiles for their icy mantles. Finally we explain how we construct models for the interiors of Uranus and Neptune with the Concentric MacLaurin Spheroid (CMS) method. We follow Militzer (2024a) when we incorporate results from atomistic *ab initio* simulations into planet-scale CMS calculations to propose models for the interior structures of Uranus and Neptune that are consistent with existing gravity measurements and compatible with the proposed convective regimes.

In the Results section, we report our findings from of all three methods. Our calculations predict the outer hydrogen-helium layers of Uranus and Neptune to be hotter than earlier models assumed. Conversely, our adiabats of liquid and superionic water much shallower in pressure-temperature space than earlier predictions, which means that we predict the deep interiors of Uranus and Neptune to be 30% colder than earlier models. If we change the model assumptions and assume there is an offset in temperature between liquid and superionic adiabats because of latent heat release, the deviation from earlier models reduces to 15%. Finally, we conclude by discussing the implications of the proposed colder interiors for future research on ice giant planets.

2. METHODS

2.1. *Para and Ortho Hydrogen*

In the outer atmospheres of giant planets, hydrogen and helium behave like ideal gases. While interaction effects can be neglected, internal degrees of freedom of the hydrogen molecules matter, which renders the difference between para and ortho hydrogen important. The para state is the ground state. It is not degenerate, its nuclear spin wave function is antisymmetric ($S = 0$), and its rotational wave function is symmetric, which implies that only states with even rotational quantum number J can be occupied. Conversely, ortho hydrogen has a symmetric nuclear spin wave function ($S = 1$) with degeneracy $2S + 1 = 3$. Its rotational wave function is antisymmetric and only states with odd J can occupied. The para-to-ortho ratio is temperature dependent, as the corresponding eigenstates have different energies, but a temperature of 166.1 K in Jupiter's atmosphere is already high enough for the para-to-ortho ratio to approach its high-temperature limit of 1:3. The conversion between para and ortho states is slow because collisions between molecules typically do not flip nuclear spins. So when measurements in giant planet atmospheres found the para-to-ortho ratios to deviate

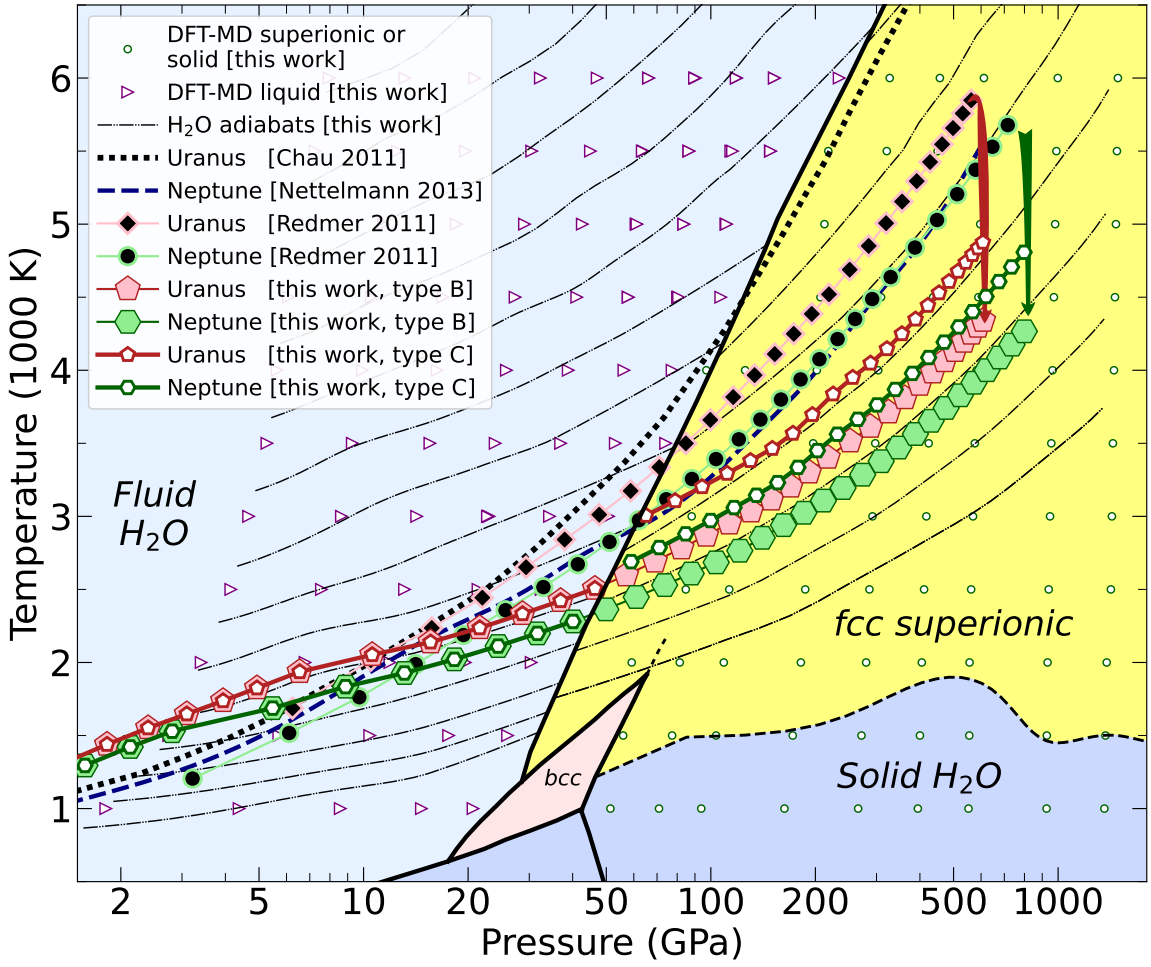

Figure 1. Pressure-temperature profiles from various models for the interiors of Uranus and Neptune are plotted over the phase diagram of H_2O that was constructed by combining results from Prakapenka et al. (2021) and Wilson et al. (2013). The slope of the adiabats (dash-dotted lines) that we derived with *ab initio* free energy calculations (triangles and circles) are much shallower than previous predictions by Chau et al. (2011) and Nettelmann et al. (2013). The arrows emphasize that the temperatures of our continuous adiabats (models of type B) at the core-mantle boundaries are ∼1400 K lower than predicted by Redmer et al. (2011). The deviations would have been even larger if Redmer et al. (2011) had not begun their adiabats at a 400 K lower temperature at 3 GPa. For this pressure, our models predict higher temperatures of 1630 and 1540 K for Uranus and Neptune, which is a result of differing adiabats in the hydrogen-helium layer in Fig. 4. Our models of type C assume that the liquid-to-superionic transition introduces a step into adiabats because of latent heat release.

from the equilibrium value, they provide an estimate for the speed of convection that brought up gases from deep and hotter regions.

Overall one may assume the atmosphere of a giant planet be in thermal equilibrium. To characterize its state, we follow the work by Saumon & Chabrier (1991). Molecular hydrogen has 46 bound electronic states, α. Each has many vibrational states, m, and rotational states, J (Huber 2013). Their energies have been carefully characterized (NIST 2025):

$$\epsilon(\alpha, m, J) = T_e + \omega_e(m+\tfrac{1}{2}) - \omega_e x_e \left(m+\tfrac{1}{2}\right)^2 + B_e J(J+1) - D_e J^2(J+1)^2 - \alpha_e(m+\tfrac{1}{2})J(J+1), \quad (1)$$

where T_e is the electronic groundstate energy, ω_e the first vibrational constant, $\omega_e x_e$ the second vibrational constant, B_e the rotational constant, D_e the centrifugal distortion constant, and α_e is the rotational constant. They all depend slightly on α (NIST 2025). In equilibrium one does not need to treat para and ortho hydrogen as separate species but can instead write down a single partition function that includes both nuclear spin states $S = 0$ and 1 with their corresponding degeneracy factors of $g = 1$ (Σ_g and even J; Σ_u and odd J), $g = 3$ (Σ_g and odd J; Σ_u and even J), and $g = 4$ (electronic states Π and Δ):

$$Z = \sum_{\alpha,m,S,J} g(\alpha, J)\ (2J+1)\,\omega_{\alpha m}\, e^{-\epsilon(\alpha,m,J)/k_B T} \quad . \tag{2}$$

where the factor $(2J+1)$ represents the multiplicities of rotational states. The factor $\omega_{\alpha m}$ represents the occupation probabilities for given electronic and vibrational states, α and m. The sum can be simplified because even J only contribute to para states with $S = 0$ and odd J only matter for ortho states with $S = 1$. From this partition function, we can derive the internal energy, entropy, and compute the para and ortho fractions as a function of temperature. We have made our source code for this calculation available (Militzer 2025a), which includes the translational degrees of freedom and allows one to compute the equation of state of a hydrogen-helium mixtures in the atmospheres of giant planets. Under those conditions, one finds that most states in Eq. 2 have too high energies to be occupied and this calculation reduces to a sum over a surprisingly small number of states. Most importantly, Eq. 2 enables one to compute an absolute entropy to anchor the adiabats for the outer layers of giant planets under low density conditions where it is impractical to perform *ab initio* simulations. The two following sections discuss them in detail because they are the preferred tool to characterize materials at high pressure.

2.2. *Ab initio simulations*

To characterize H_2O in the mantles of Uranus and Neptune, we performed density functional molecular dynamics (MD) simulations with the Vienna *Ab Initio* Package (VASP) (Kresse & Furthmüller 1996). We employed the Perdew, Burke, and Ernzerhof functional (Perdew et al. 1996) and used hard pseudo-potentials with the projector augmented-wave (PAW) method (Kresse & Joubert 1999). The valence configurations for the atoms were O([He]$2s^2 2p^4$) and H($1s^1$). Following Wilson et al. (2013), all simulations employed 144 atoms. Liquid simulations used cubic cells of the appropriate volumes. For the superionic simulations with face-centered cubic oxygen sublattice, we constructed monoclinic but nearly cubic supercells with parameters $a = b$, $c/a = 1.095$, $\alpha = \beta = 90°$, and $\gamma = 78.5°$ (Militzer 2016). We consistently employed a 2×2×2 Monkhorst-Pack grid to sample the Brillouin zone. The electronic wave functions were expanded in a plane-wave basis with an energy cut-off of 900 eV. All molecular dynamics simulations used a time step of 0.2 fs to accommodate the motion of the light hydrogen nuclei. The temperature of our NVT ensembles was regulated by a Nosé-Hoover thermostat (Nosé 1984).

2.3. *Thermodynamic integration*

The entropy is a measure of the total number of microstates in an ensemble and is thus not directly accessible with MD and MC simulations, which only construct a representative subset of microstates and do not attempt to perform an integration over all states. On the other hand, MD and MC method

are very good in calculating free energy differences between two similar ensembles via thermodynamic integration, which enables one to indirectly derive the entropy, S, from $S = (E-F)/T$, where E and F are the internal and Helmholtz free energies. Like pressure, the internal energy can be derived from a single MD or MC simulation (Allen & Tildesley 1987). Gaining access to the free energy requires one to construct a thermodynamic integration path (de Wijs et al. 1998) from a state of known free energy, F_{id}. For liquids, we choose an ideal gas and, for solids, we use an Einstein crystal, in which every particle is tethered to a particular lattice site. The integration should be stable and efficient, which is why we employ the following two-step integration procedure (Morales et al. 2009; Wilson & Militzer 2012a,b; Militzer 2013; Wahl et al. 2013; González-Cataldo et al. 2014; Wahl & Militzer 2015) to derive the Helmholtz free energy, F, of the DFT system for given temperature, volume, and particle number,

$$F_{DFT} = (F_{DFT} - F_{PP}) + (F_{PP} - F_{id}) + F_{id}\,, \tag{3}$$

$$= \int_0^1 d\lambda \,\langle U_{DFT} - U_{PP}\rangle_\lambda + \int_0^1 d\lambda \,\langle U_{PP} - U_{id}\rangle_\lambda + F_{id}\,. \tag{4}$$

The angular brackets represent an average for a single λ value that was computed by sampling particle configurations according to a hydrid potential energy function, $U_\lambda(r) = U_a(r) + \lambda(U_b(r) - U_a(r))$. Because DFT simulations are orders of magnitude more expensive than calculations with pair potentials (PP), one wants the first integration step in Eq. 3 to be most efficient so that only a few integration steps are needed and the average of $U_{DFT} - U_{PP}$ converges quickly. For given temperature, volume, and composition, we perform a preliminary DFT-MD simulation and fit a pair potential to the computed DFT forces (Izvekov et al. 2003). In this process, three points need to be considered:

(1) For solids, the pair potentials and the Einstein potentials contribute to holding particles in place while their combined forces should match the DFT forces. So we choose pair and Einstein potentials such that each contribute approximately half. For every atom type, we derive a harmonic force constant, k, from $3/2k_BT = k/2\,(\vec{r}_i(t) - \vec{r}_i^{\,0})^2$ where $\vec{r}_i(t)$ marks the position of particle i and $\vec{r}_i^{\,0}$ is its position in a perfect lattice. We then lower k by 50%, subtract Einstein forces from the DFT forces, and fit a pair potential to the remaining forces. For liquids, pair potentials are fitted to the unaltered DFT forces.

(2) Atoms repel each other strongly at close range because of Pauli exclusion effects and Coulomb repulsion. There are for example no pairs of oxygen atoms in the simulation in Fig. 2 that are closer than 1.9 $\mathring{A}$. The fitted pair potentials thus need to be extrapolated towards small distances. The extrapolated part of the pair potentials are not invoked in the first integration step in Eq. 3 but they become important in the second where we gradually turn off the pair potentials. For liquids, the limit $\lambda \to 0$ is equivalent to the limit of infinite temperature where particles are uniformly distributed and the average pair potential energy and its λ derivative are given by

$$\langle U_{PP}\rangle_{\lambda=0} = \frac{4\pi}{V}\int dr\, r^2\, U_{PP}(r) \quad \text{and} \quad \left.\frac{\langle U_{PP}\rangle}{d\lambda}\right|_{\lambda=0} = \beta\,\langle U_{PP}\rangle^2 - \beta\,\langle U_{PP}^2\rangle \quad \text{with} \quad \beta = 1/k_BT\,. \tag{5}$$

The integrals are finite because we construct our potentials so that they go to zero for large distances. In the limit of high temperature, the particles become arbitrarily close, for which typical DFT codes cannot construct electronic orbitals. This is another reason for why we first switch from DFT to

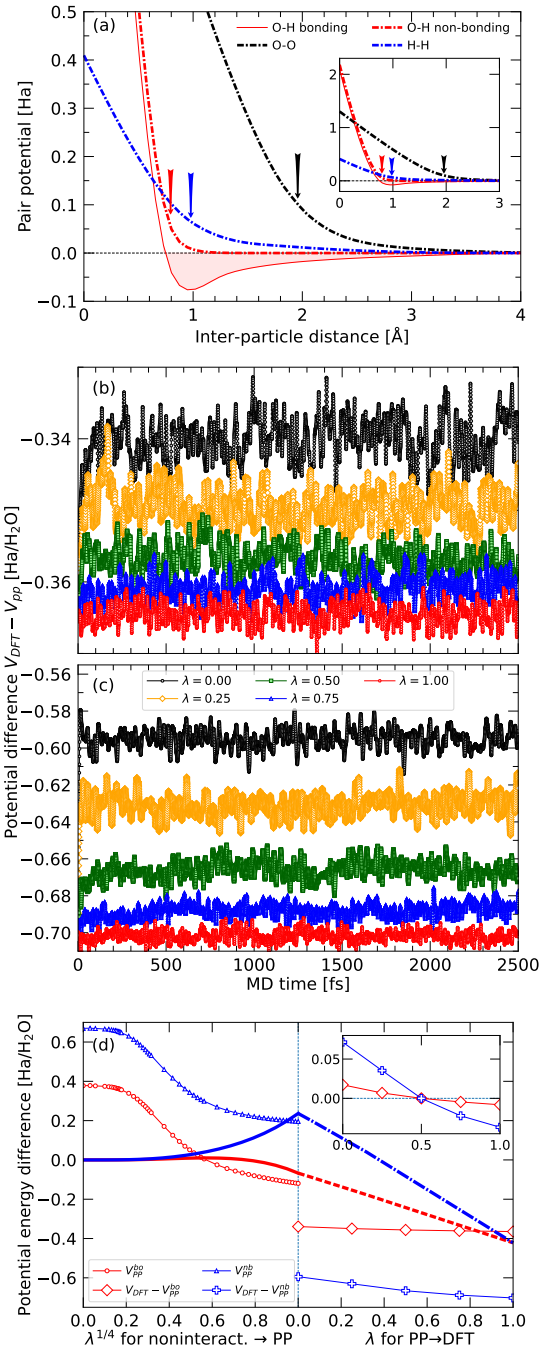

Figure 2. Panel (a) shows pair potentials between O and H atoms that were derived from a simulation of liquid H_2O at 3000 K, 1.75 g cm^{-3}, and 23 GPa. The arrows mark the beginning of the extrapolation towards smaller distances for each pair of atom types. For bonding and nonbonding pair potentials, panels (b) and (c) display the DFT and pair potential energy as function of MD time. Their time averages are represented by the diamond and plus symbols on the right side of panel (d). In the inset, we subtracted their respective λ=0.5 value from both functions to better compare changes in their magnitudes. The purpose of panel (d) is illustrate that one obtains the same integral when one performs the thermodynamic integration with bonding and nonbonding potentials. On the left side, we plot the average pair potential energies as function of $\lambda^{1/4}$ that we derived classical MC calculations. Their integrals over λ are represented by the two thick lines. On right side, dashed and dot-dashed lines continue the integration into the regime where we switch from pair potentials to DFT forces. At $\lambda = 1$, both lines converge to -0.42 Ha/H_2O emphasizing that both integration methods yield consistent results.

pair potentials in Eq. 3. During construction, we extrapolate out pair potentials linearly to small distances (see Fig. 2) so that the value of $\langle U_{PP} \rangle_{\lambda=0}$ in Eq. 5 remains finite.

(3) Pair potentials cannot accurately represent the nonadditive many-body forces in hot, dense liquids and solids. However, Eq. 3 yields exact results as long as the ensembles generated by the DFT and by PP potentials are not too different, which can become an issue for strongly bonded, molecular fluids like hydrogen (Militzer 2013). The pair potentials will accurately represent the strong intramolecular H_2 bond but then indiscriminately applies it to all pairs of atoms neglecting all intermolecular repulsion, which leads to the formation of unphysical clusters because no many-body bonding effects are considered. To prevent such instabilities, we follow Soubiran & Militzer (2015) and remove the attractive part from the pair potentials by setting it constant beyond the first potential minimum. Then we uniformly shift the potential up so that approaches zero for large distances, as we show in Fig. 2.

2.4. *CMS Calculations and Planetary Interior Models*

Following Nettelmann et al. (2013), we adopted for Uranus and Neptune the equatorial radii of 25559 and 24766 km, planet masses of 14.536 and 17.148 Earth masses, rotation periods of 17:14:40 and 16:06:40 hours and 1 bar temperatures of 76 and 72 K. The target values for gravitational moments were $J_2 \times 10^6 = 3510.99 \pm 0.72$ and 3529 ± 45 as well as $J_4 \times 10^6 = -33.61 \pm 1$ and -35.8 ± 2.9 as determined by the Voyager 2 spacecraft. We calculate these moments with,

$$J_n = -\frac{4\pi}{Ma^n} \int_0^1 d\mu \int_0^{r_{\rm max}(\mu)} dr \; r^{n+2} \; P_n(\mu) \; \rho(r,\mu) \quad , \tag{6}$$

from the planet's interior density that we represent a function of radius, r, and $\mu = \cos(\theta)$, the cosine of colatitude. P_n are Legendre polynomials, M is the planet's mass and a its equatorial radius.

We construct models of the interior structure of Uranus and Neptune with the accelerated version (Militzer et al. 2019) of the nonperturbative Concentric MacLaurin Spheroid (CMS) method (Hubbard 2013), which represents the interior of these rotating planets by a series of $N_S = 512$ axisymmetric spheroids. Their shapes are adjusted until a state of hydrostatic equilibrium is established that takes into account gravitational and centrifugal forces. The rotation period and the equatorial radius are reproduced by construction but matching the planet's total mass requires some discussion. Hubbard & Militzer (2016) adjusted the density of the innermost spheroid to match Jupiter's total mass. Militzer et al. (2022) and Militzer & Hubbard (2024) varied the heavy element abundances of the outer and inner layers to match Jupiter's mass and J_2. To match the total mass of Uranus and Neptune, we scale the equatorial radii of the three inner layers, r_1, r_2, and r_3 as the CMS method converges to a hydrostatic solution.

As illustrated in Fig. 3, we followed Militzer (2024a) by constructing interior models with four layers: 1) a protosolar mixture of hydrogen and helium, 2) mixture of H_2O and hydrogen, 3) carbon-nitrogen-hydrogen mixture and 4) the rocky core composed of iron and rock. We introduce the parameters H_1, H_2, and H_3 to characterize the following hydrogen fractions. We assume our ocean layer to be homogeneous and convective, with $H_1 = N_H/2N_O$ defining its hydrogen fraction in terms of the number of hydrogen and oxygen nuclei, N_H and N_O. We assume that the carbon-nitrogen-hydrogen layer is stably stratified because it hydrogen contents vary between H_2 at the top and H_3

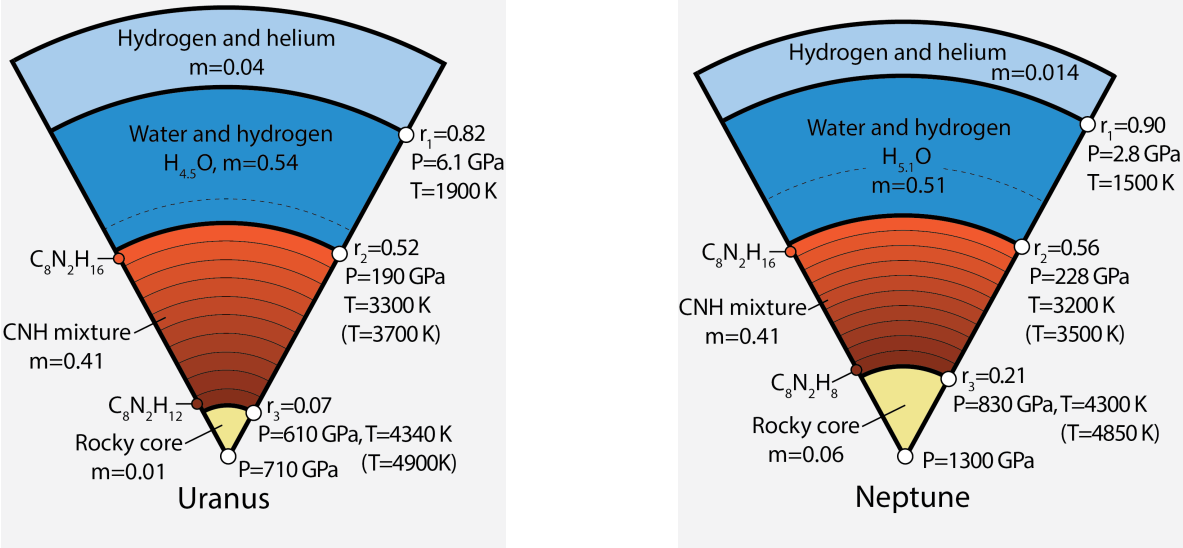

Figure 3. Two representative interior models for Uranus and Neptune with four layers: 1) hydrogen and helium, 2) H_2O and hydrogen, 3) carbon-nitrogen-hydrogen mixture and 4) the rocky core composed of iron and rock. m specifies the fractional layer masses. The temperatures for B and C type models are printed without and with parenthesis. The dashed lines in the second layer mark the conditions for the transition from liquid to superionic in pure H_2O.

at the bottom. $H_{2,3} = N_H/(4N_C + 3N_N)$ are defined in terms of the number of carbon and nitrogen atoms in the mixture, N_C and N_N.

To reduce the discretization error, we slightly adjust the grid of the equatorial spheroid radii so that every layer boundary coincides with a grid point (Militzer 2024a). We compared results of CMS calculations with 256 and 512 spheroids and found that the change in the predicted gravity coefficients is small. (Bailey & Stevenson (2021) employed only $N_S = 30$ spheroids for their Uranus and Neptune models.) Scaling the radii r_1, r_2, and r_3 enables us derive a valid interior model of the expected mass even in situations where one of these three layers is rather small. This also means that we have removed one dimension from our Markov chain Monte Carlo (MCMC) calculations (Militzer 2023a, 2025b) and now have five independent parameters, r_2/r_1, r_3/r_1, H_1, H_2, and H_3 that are constrained to satisfy $1 \le r_2/r_1 \le r_3/r_1 \le 0$ and $H_2 > H_3$. The MC algorithm is designed to generate ensembles of models by sampling from the probability density, $\exp(-\chi^2/2)$, where χ^2 represents the deviation in the gravity coefficients between the observations and model predictions that were computed with Eq. 6,

$$\chi^2 = \sum_{n=1}^{2} \left(\frac{J_{2n}^{\rm model} - J_{2n}^{\rm obs}}{\delta J_{2n}^{\rm obs}} \right)^2 \quad . \tag{7}$$

$\delta J_{2n}^{\rm obs}$ are one sigma error bars.

Step by step the CMS algorithm (Hubbard 2013) converges to a hydrostatic interior structure by repeatedly looking up information in the *ab initio* EOS tables. For example, the spheroid shapes are employed to compute the potential on all spheroid surfaces that represents gravitational and centrifugal forces. From these potential values, one derives updated values for the pressure on all

spheroids. For a given layer and composition, one derives the temperature that correspond to a pressure by assuming an isentrope of known entropy. Then one looks up the corresponding density in the EOS table for given pressure, temperature, and composition. The updated density profile is then inserted into the CMS calculation to revise all surface potentials, which enables one to update the spheroid shapes and pressure values. We typically update the pressure values more frequently than the spheoriod shapes because it allows us to converge to a self-consistent hydrostatic structure more efficiently.

3. RESULTS

3.1. *Hydrogen-helium layer*

Table 1. Relationship of pressure, temperature and density for isentropes of the three giant planets that were derived with Eq. 2 for hydrogen-helium mixture with plausible helium mass fractions, Y, that are stated in column 1. Column 5 lists the entropy per particle, N ($N = N_{\rm H_2} + N_{\rm He}$ for hydrogen molecules and helium atoms). In column 6, we list the related entropy per electron, $S^-/{\rm el} = [S/N]/2 - \Delta S \times N_{\rm H_2}/N$. The last three columns provide the fraction of para hydrogen and the fractional occupation of the first and second vibrational energy levels, $m = 0$ and 1.

Planet	P [bar]	T [K]	ρ [g cm^{-3}]	S [k_B/N]	S$^-$ [k_B/el]	$f_{\rm para\,H}$	occ m=0	occ m=1
Neptune	1	72.00	0.000391	12.635	5.737	0.5434	1.000	0.000
Y=0.2777	10	145.13	0.001937	12.635	5.737	0.2910	1.000	0.000
	100	298.71	0.009414	12.635	5.737	0.2507	1.000	0.000
	1000	594.50	0.047299	12.635	5.737	0.2500	1.000	0.000
	10000	1166.54	0.241047	12.635	5.737	0.2500	0.994	0.006
Uranus	1	76.00	0.000370	12.834	5.836	0.5128	1.000	0.000
Y=0.2777	10	154.82	0.001816	12.834	5.836	0.2818	1.000	0.000
	100	317.18	0.008865	12.834	5.836	0.2505	1.000	0.000
	1000	630.75	0.044581	12.834	5.836	0.2500	1.000	0.000
	10000	1234.08	0.227855	12.834	5.836	0.2500	0.992	0.008
Jupiter	1	166.10	0.000166	15.346	7.074	0.2736	1.000	0.000
Y=0.238	10	336.96	0.000816	15.346	7.074	0.2503	1.000	0.000
	100	665.98	0.004128	15.346	7.074	0.2500	1.000	0.000
	1000	1291.94	0.021278	15.346	7.074	0.2500	0.990	0.010
	10000	2355.50	0.116708	15.346	7.074	0.2500	0.915	0.077

We begin by discussing the temperature profile of Uranus and Neptune's outer hydrogen-helium layer. We assume an isentrope with a protosolar helium fraction of Y=0.2777 and neglect minor species such as methane. In Fig. 4, we compare the temperature profiles from Eq. 2 with other calculations. In Tab. 1, we state the anchor points at 1 bar for the isentropes of different planets. For all

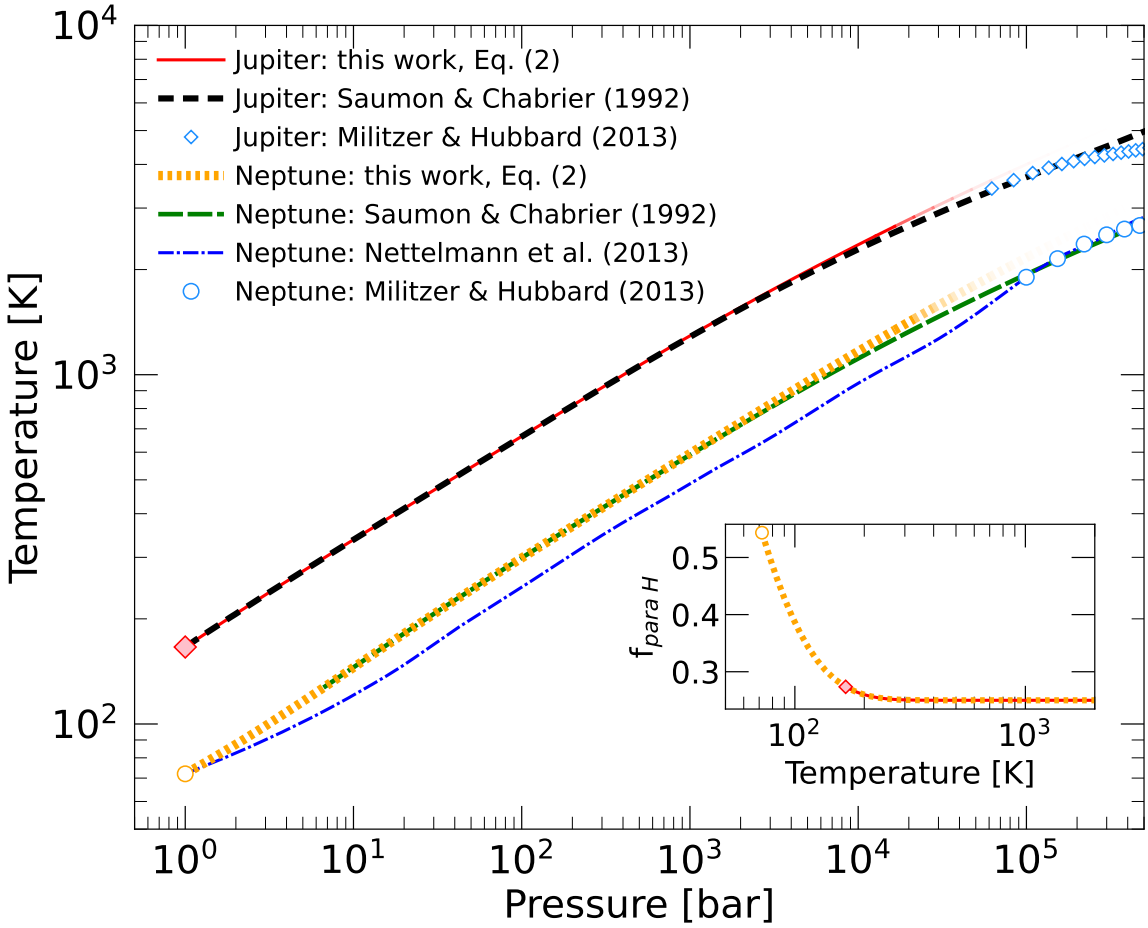

Figure 4. Isentropes of hydrogen-helium mixtures in the outer layers of Jupiter and Neptune. The symbols at 1 bar mark the anchor points with temperatures of 166.1 and 72 K respectively. The inset shows the fraction of para hydrogen, which approaches 1/4 in the limits of high temperature.

higher pressures, the density and temperature were adjusted until the target pressure and the entropy of the anchor point were reproduced. What one might consider to be a complex statistical problem of atomic physics greatly simplifies under the conditions in the outer envelopes of giant planets where the temperature is too low for many molecular eigenstates to be occupied. For example, none of the excited electronic states matter because already the first excited state requires an excitation energy of 11.4 eV or 132 000 K. Furthermore, the last two columns of Tab. 1 show that only the lowest vibrational energy is occupied unless the temperature reaches ∼1000 K, at which the occupation fraction of the vibrational $m = 1$ state reaches about 0.3%. This bring us to the rotational states, which require the least excitation energy of ∼170 K. Even for those, the corresponding sum in Eq. 2 converges rapidly. For a temperature of 1000 K, just 12 rotational states are required to compute the entropy with an accuracy of 10^{-4} k_B/particle. The inset of Fig. 4 shows the fraction of para hydrogen, which will approach 1 in the limit of low temperature. By 300 K, the para-to-ortho ratio has already converged its high-temperature limit of 1:3 ($f_{\mathrm{para\,H}} = 1/4$). At 1 bar, the para fraction of Uranus and Neptune's atmosphere is about 50%, while it is about 27% for Jupiter because its atmosphere is hotter.

In Fig. 4, we compare the isentrope predicted by Eq. 2 with results in the literature. For pressures up to 5 kbar, we find excellent agreement with the work by Saumon & Chabrier (1992) (SC), for which a code is available that interpolates precomputed tables for temperatures greater than 125 K. To make such calculations more accessible and to extend them to lower temperatures, we make our source code available (Militzer 2025a). For pressures exceeding 5 kbar, the interaction between particles that we have neglected in Eq. 2 start to matter. Saumon & Chabrier (1992) included different types of interactions into their EOS tables, which reduce the temperature of an isentrope. At a pressure of 100 kbar (10 GPa), their predictions converged to the results from *ab initio* simulations from Militzer & Hubbard (2013) (MH13) for Neptune and Jupiter as Fig. 4 shows.

For the comparison between *ab initio* simulations and analytical methods like Eq. 2 to be meaningful, one needs to agree on a definition for the entropy and both methods need to be able to provide absolute entropies. The *ab initio* entropies of MH13 were derived with a TDI method that relied on classical nuclei and quantum mechanical forces and therefore does not include any spin effects of the hydrogen nuclei. This is perfectly reasonable at high pressure where the nuclear spin states do not affect the motion of the atoms. In the weakly coupled regime at low pressure, nuclei spin effects need to be considered because they affect the rotational states of the hydrogen molecules. The simplest way to make the *ab initio* entropies of MH13 compatible with entropies of Eq. 2 and of SC EOS is to add $\Delta S = k_B \ln(2)$ per hydrogen atom to the MH13 entropies to incorporate the missing nuclear spin degrees of freedom. If one does not want to alter the MH13 entropies for some reason one may subtract ΔS per atom from all entropies that were computed with Eq. 2 (see S^- in Tab. 1). This subtraction allows one to compare the entropy values and to align the isentropes in P-T space but it would not yield a proper thermodynamic entropy because it would approach $-\Delta S$ in the limit of low temperature.

Fig. 4 shows that the SC predictions for Jupiter start to deviate from the *ab initio* simulations above 200 kbar because molecules start to interact strongly and one approaches the regime of pressure driven molecular dissociation, which SC model interpolates across. More details are provided in Guillot et al. (2004); Militzer & Hubbard (2007); Militzer et al. (2008).

Fig. 4 also shows that the Neptune model by Nettelmann et al. (2013) predicts temperatures that are ∼20% lower than other predictions over a wide range of pressure from 10 bar to 20 kbar.

3.2. *TDI for liquid water*

In Fig. 2, we compare the results from two different TDI calculations for liquid water at 3000 K, 1.75 g cm^{-3}, and 23 GPa. Panel (a) shows that only the O-H potential has an attractive part, which we have removed when we constructed our set of nonbonding potentials while the O-O and H-H were the same as in our set of bonding potentials. Panels (b) and (c) demonstrate that TDI simulations with bonding and nonbonding pair potentials are stable for all λ values. The ensemble generated with the nonbonding potentials differs more from the DFT ensemble as the inset of panel (d) illustrates. For the nonbonding potentials the integrand, $\langle U_{DFT} - U_{PP} \rangle_\lambda$, has more curvature and the difference between λ=0 and 1 points is 0.11 Ha/cell while it is only 0.025 Ha/cell for our bonding potentials, which makes the time consuming evaluation of the first term in Eq. 3 more efficient.

With the bonding potentials, we obtained an entropy of 21.97±0.26 k_B/H_2O while we derived 22.04±0.30 with the nonbonding potentials. (An error bar of 0.3 k_B/H_2O translates into a small temperature uncertainty of only 11 K.) Both results are consistent with each other, which we further analyze in panel (d) of Fig. 2. On the left side, we compare the two $\langle V_{PP} \rangle_\lambda$ curves (red and blue

symbols). They have similar but not identical shapes. The average potential energy, $\langle V_{PP} \rangle_\lambda$ is higher for the nonbonding potentials because we shifted U_{O-H} up when we removed the attractive part of the potential. The integral $\int_0^1 d\lambda \langle V_{PP} \rangle_\lambda$ (solid blue line) is thus larger than that of the bonding potential (red solid line). But when we add the integral $\int_0^1 d\lambda \langle V_{DFT} - V_{PP} \rangle_\lambda$ in the right figure panel, results with both pair potentials converge to the same value of -0.42 Ha/H_2O at $\lambda = 1$. This confirms that one obtains consistent results for different classical potentials, which is one of the main strength of the TDI method.

3.3. *Isentropes of liquid and superionic H_2O*

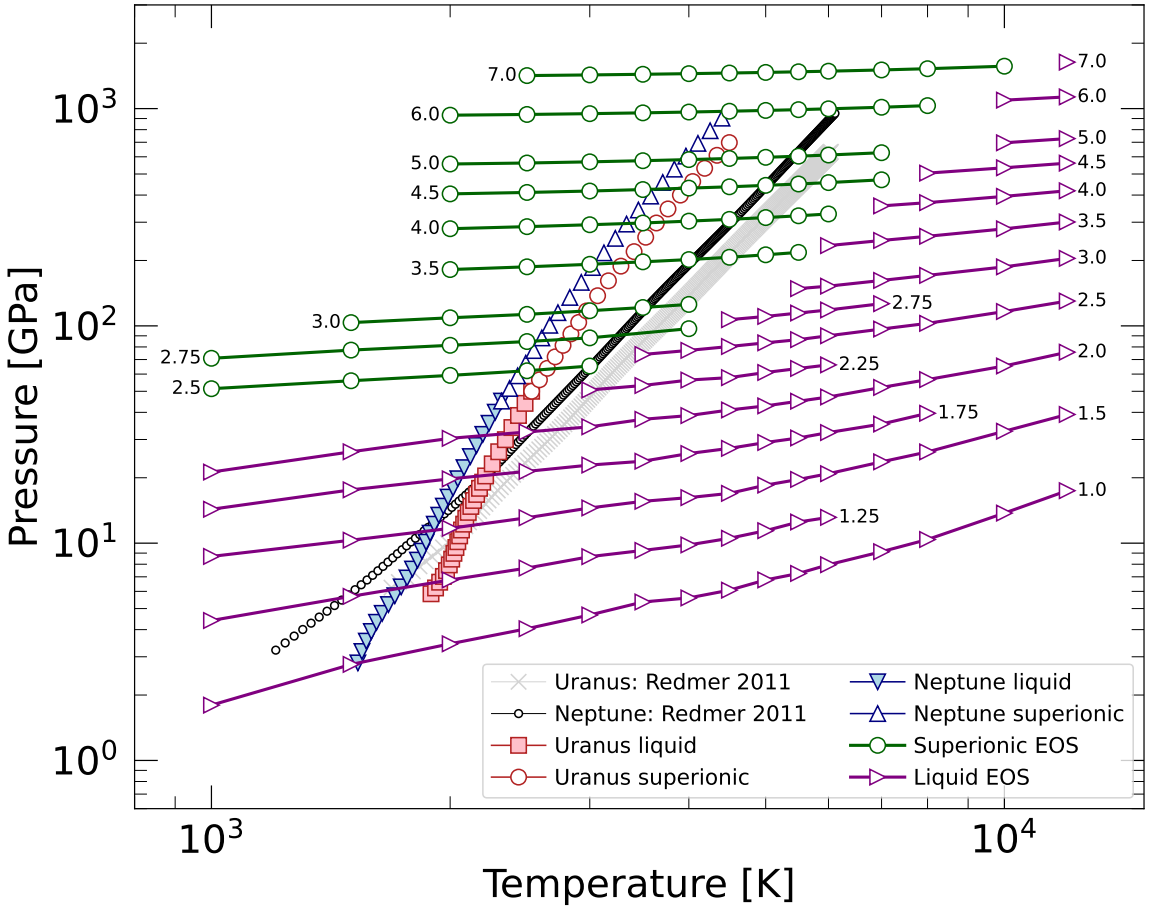

Figure 5. Pressure for isochores of liquid and superionic H_2O. The labels specify the density in g cm^{-3}. The offset between the two families of curves implies a first order phase transition. For given density and temperature, the pressure of the liquid phase is higher than that of the superionic phase, which implies the melting line has a positive slope $dP/dT > 0$. The temperature-pressure profiles of our interior models for Uranus and Neptune of type B are compared with the much hotter conditions proposed by Redmer et al. (2011).

In Figs. 5 and 6, we plot the pressure that we derived with our *ab initio* simulations over a wide range density and temperature conditions that include the interiors of Uranus, Neptune, and far beyond as we illustrate in Fig. 1. Our equation of state table is available at Militzer (2025c).

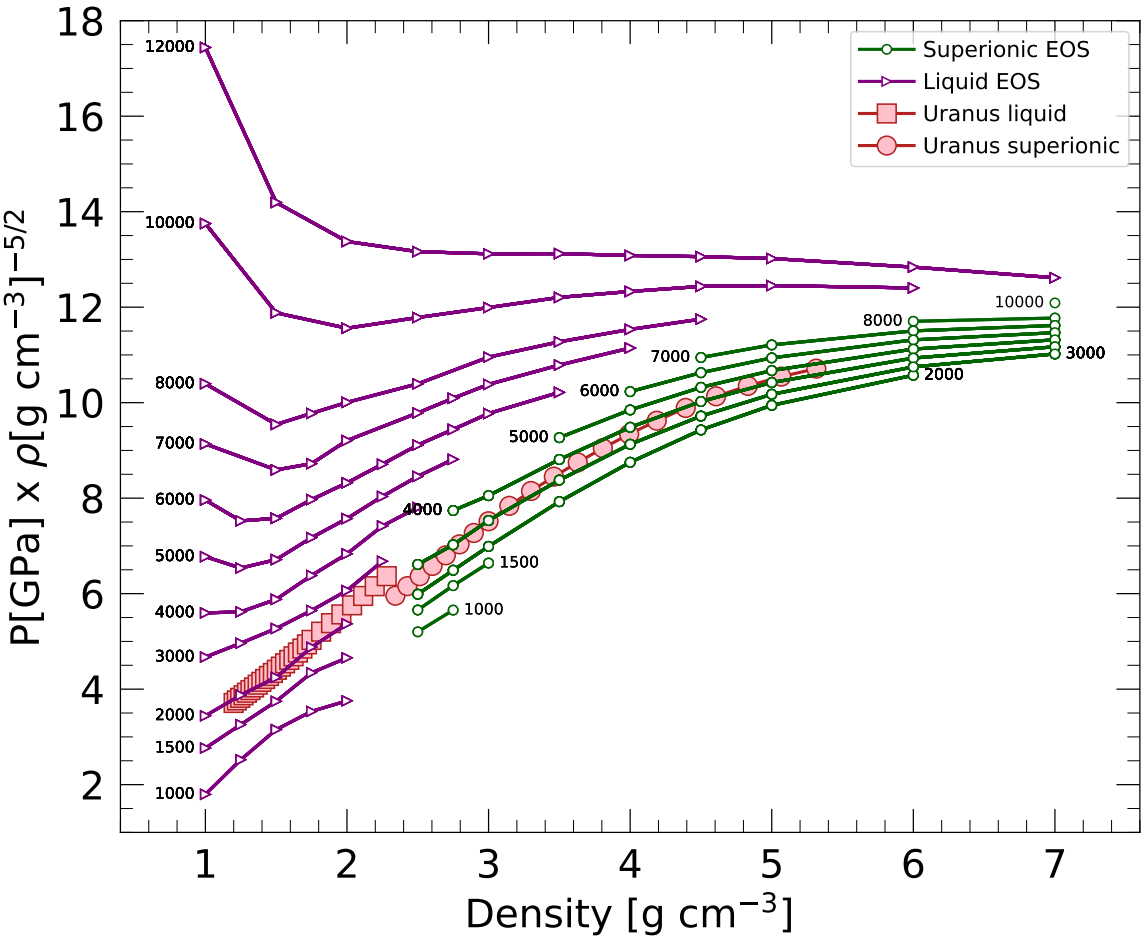

Figure 6. Pressure of liquid and superionic H_2O is plotted as function of density for different temperature values that are specified on every curve in units of Kelvin. For clarity, we multiplied the pressure by density to the power of $-2/5$ because pressure varies strongly with density. Our Uranus model of type B from Fig. 3 is included.

There is an offset in pressure between the liquid and superionic branches as the 2.5 and 2.75 g cm^{-3} isochores in Fig. 5 illustrate. This implies the melting transition of superionic ice is a first-order phase transition. It has a positive dT/dP Clapeyron slope because the superionic phase is denser. This is confirmed by the offset in pressure between the 3000 and 4000 K isotherms in Fig. 6.

A first-order phase transition also implies a discontinuous change in entropy as we illustrate in Figs. 7 and 8 where we plot *ab initio* entropies that we derived for both phases. Because oxygen atoms are more ordered in the superionic structure, this phase has lower entropy, which can be seen best by following the 2000, 3000, and 4000 K isotherms in Fig. 6. So if a parcel of fluid H_2O transitions into the superionic state, it would release latent heat and its density would decrease.

3.4. *Implications for Uranus and Neptune*

Figs. 1 and 5 show that our *ab initio* derived isentropes are much shallower in pressure-temperature space than those proposed earlier. At any point, their slopes can be expressed in terms of $\delta = \frac{\partial \ln T}{\partial \ln P}|_S$ and Grüneisen parameters $\gamma_G = \frac{\partial \ln T}{\partial \ln \rho}|_S$. If one considers a pressure or density range, one can introduce effective values for these coefficients by fitting $T \propto P^\delta$ and $T \propto \rho^{\gamma_G}$. For an ideal gas

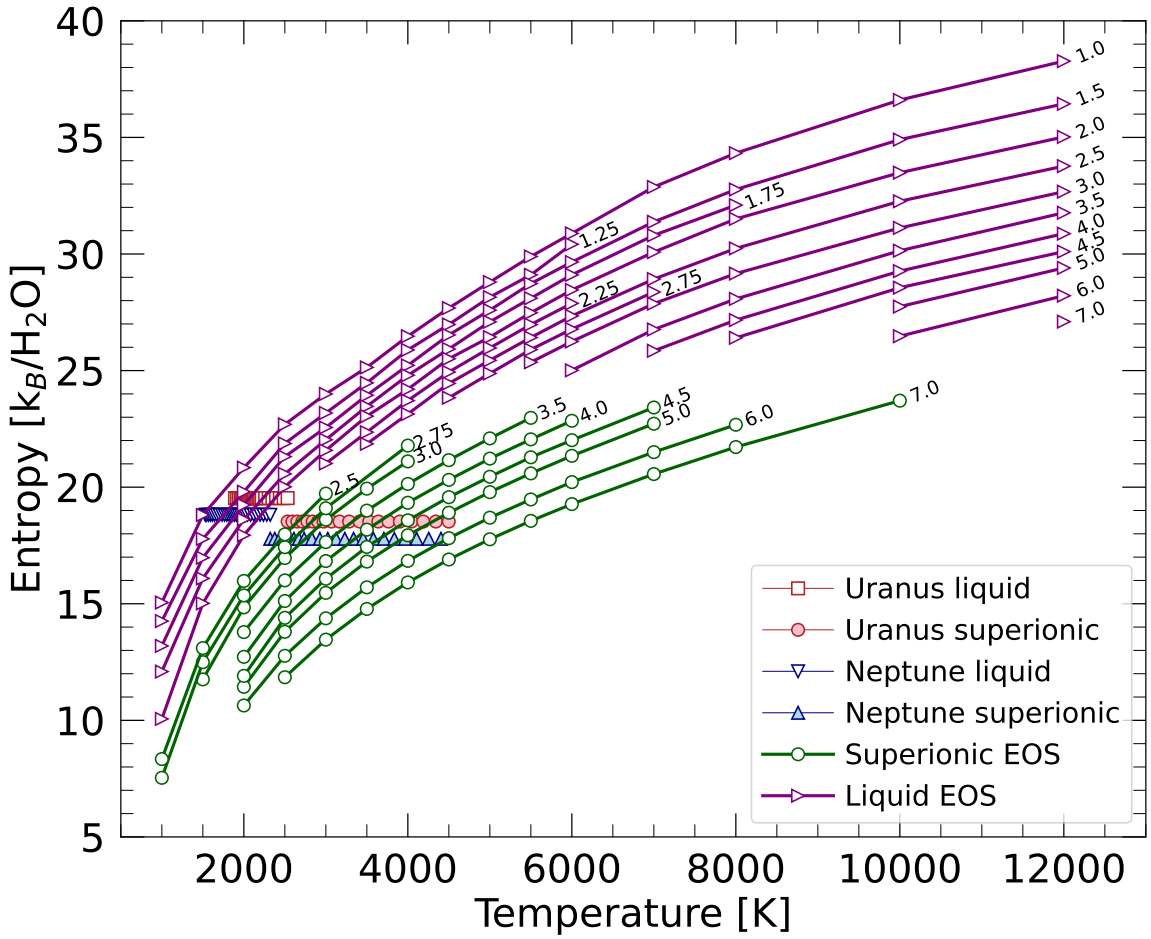

Figure 7. Entropy of liquid and superionic H_2O that we computed for different density values that are specified in units of g cm^{-3}. For given density and temperature, the entropy of liquid water is higher because the oxygen nuclei are more disordered. For reference, we mark the conditions of our two interior models of type B for Uranus and Neptune in Fig. 3.

of nonlinear, triatomic molecules, one obtains $\delta = 1/4$ and $\gamma_G = 1/3$ by assuming the vibrational degrees of freedom are frozen while the transitional and rotational motion can proceed unhindered, which is unrealistic for fluids at high pressure where interaction effects are very important.

For Uranus and Neptune conditions, we obtained $\delta \approx 0.15$ and $\gamma_G \approx 0.52$ for fluid H_2O from 3–20 GPa and $\delta \approx 0.24$ and $\gamma_G \approx 0.73$ for superionic H_2O from 130–1300 GPa. These values are much smaller than previous predictions as the slopes of different curves in Fig. 1 illustrate. Hubbard & MacFarlane (1980) assumed $\delta \approx 0.31$ and $\gamma_G \approx 0.9$ for the entire ice layer. Chau et al. (2011) assumed a similar slope of $\delta \approx 0.32$. The isentropes by Redmer et al. (2011) are consistent with a value of $\delta \approx 0.28$. The adiabat of Nettelmann et al. (2013) can be represented by $\delta \approx 0.23$ and $\gamma_G \approx 0.63$ from 10–60 GPa and by $\delta \approx 0.29$ and $\gamma_G \approx 0.82$ from 100–590 GPa.

To understand the likely implications of these shallower slopes for the interiors for Uranus and Neptune we need to introduce additional approximations because their mantles are in all likelihood not composed of pure water (Podolak et al. 1995). So we adopted the interior models from Militzer (2024a) in Fig. 3 and employed our H_2O isentropes to approximately present the temperature profiles

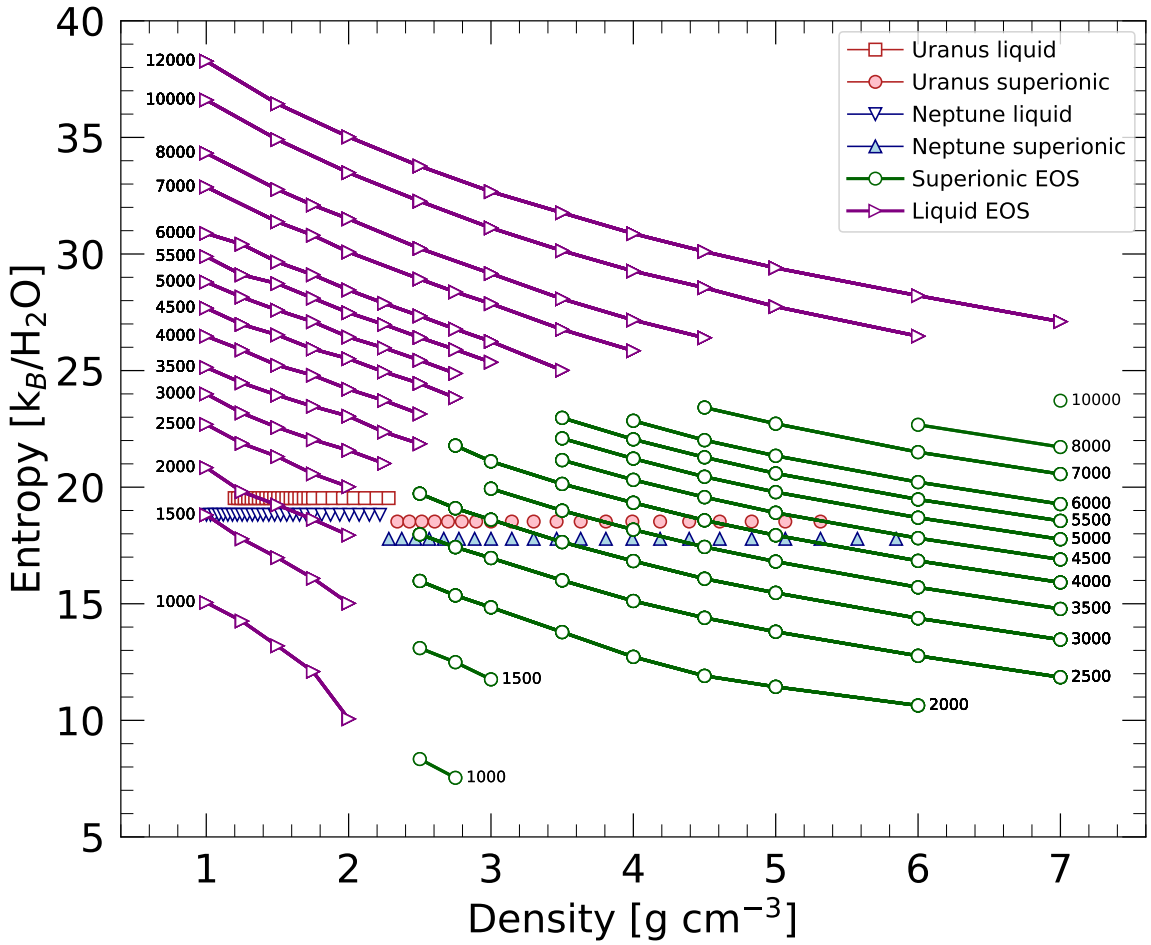

Figure 8. Entropy of liquid and superionic H_2O from Fig. 7 for different temperatures are plotted as function of density. For a given temperature, the liquid and superionic curves are offset because the oxygen nuclei are more disordered in the liquid phase. The conditions of our two interior models of type B for Uranus and Neptune in Fig. 3 are included.

of the outer water-hydrogen layer and of inner carbon-nitrogen-hydrogen layer. Even though our *ab initio* derived adiabats are colder than previously assumed, we had no difficulties constructing models that match the observed gravity fields of Uranus and Neptune. Two interior models are illustrated in Figs. 1 and 3. The corresponding data files are available at Militzer (2025c).

To characterize the plausible range of model parameters, we constructed ensembles of interior models with our MCMC methods (Militzer 2023b, 2024b). In Figs. 9, 10, and 11, we show the resulting posterior distributions for Uranus and Neptune models that we constructed with the CMS method. The single flyby of the Voyager 2 spacecraft did not constrain the gravity field of Neptune as well as that of Uranus. The resulting distributions of the gravity harmonics J_n in Fig. 9 are thus much wider for Neptune. These coefficients describe a planet's response to rotation. For nonrotating planets in hydrostatic equilibrium, all $J_{n>0}$ would be zero. In the histograms, the J_{2n} distributions of both planets overlap but in the $J_{2n} - J_{2m}$ correlation plots, the Neptune models tend to show larger J_{2m} value, which is not too surprising because as Neptune rotates a bit faster than Uranus. The signs of the J_{2n} alternate with increasing n, which is simply a consequence of how the Legendre

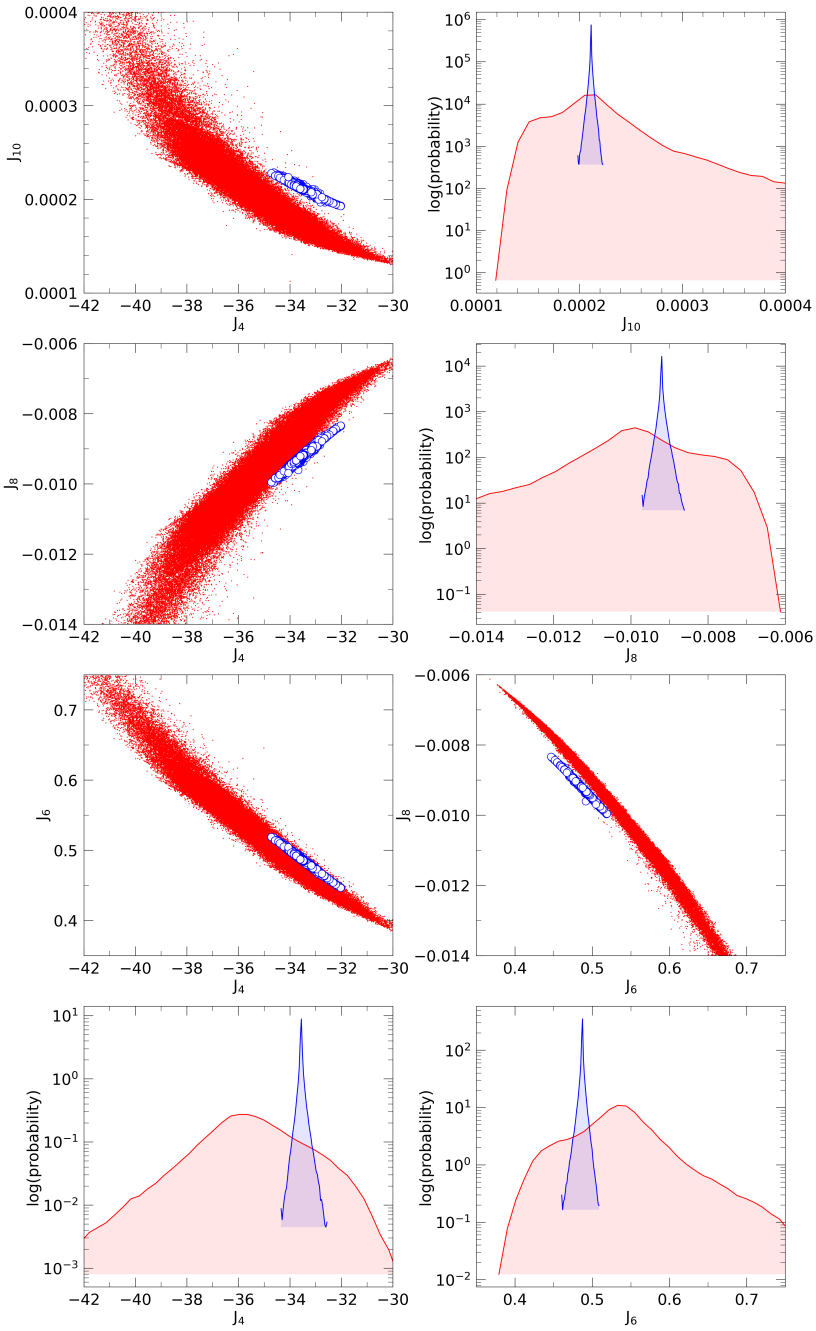

Figure 9. Posterior distributions of gravity harmonics, J_n, that we derived with MCMC calculations of the interiors of Uranus (blue) and Neptune (red). We show correlation plots and histograms. For the latter we chose a logarithmic Y axis to accommodate a wide range of probability densities. The panels were ordered so that some X axes align vertically. No dynamic contributions from winds were considered in the calculation of the J_n. Predictions for Neptune vary much more because the planet's gravity field has been measured less accurately.

polynomials are defined. If one studies just the magnitudes of the J_{2n}, one finds that they are

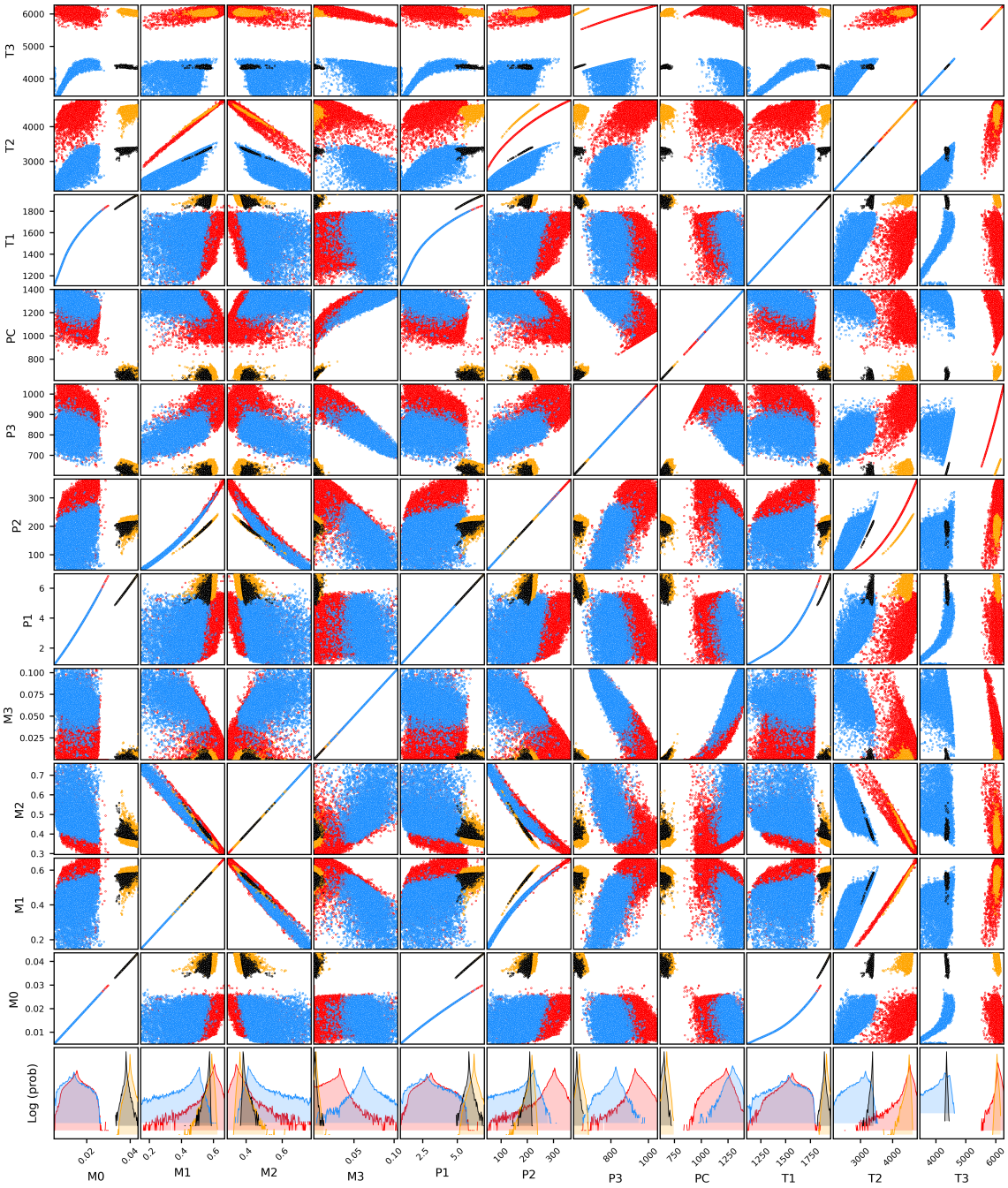

Figure 10. Posterior distributions of layer masses, boundary pressures and temperatures. M_0, M_1, M_2, and M_3 refer to the fractional masses of the four interior layers in Fig. 3: 1) H-He, 2) H_2O rich, 3) C-N-H and 4) the rocky core. P_1 in units of GPa and T_1 in K refer to the conditions of boundary between layers 1 and 2. Similarly, $P_{i>1}$ and $T_{i>1}$ characterize the boundaries between deeper layers in Fig. 3. Finally P_C refers to the pressure at the planet's very center. The blue and red points respectively represent CMS ensembles of Neptune that we constructed with our temperature-pressure profile of type B and the hotter profile that was proposed by Redmer et al. (2011) that we show in Fig. 1. Conversely the black and orange symbols shows ensembles of Uranus models with our type B and Redmer et al. (2011) temperature profiles. Our temperatures are much lower than that by Redmer et al. (2011), which affects many other planetary properties.

all positively correlated with each other in Figs. 9. So if according to one model in the MCMC ensemble, the mass distribution inside a planet responds a bit more strongly to the centrifugal forces, the magnitude of all J_{2n} increases slightly, which explains their pairwise positive correlation.

For all of our models, we assume Uranus and Neptune cool convectively and their interior temperature profiles can be represented by different isentropes. One still has to make additional assumptions for the first-order transition from liquid to superionic water that is associated with a discontinuous change in density and entropy as we discussed in the previous section. If one assumes that this transition introduces a barrier to convection then one would treat it like the boundary between the hydrogen-helium and the ocean layers where one assumes common values for pressure and temperature at the interface but then choose a different value of the entropy in both layers. The results are continuous pressure-temperature profiles as we illustrate in Fig. 3. By assuming a continuous pressure-temperature profile, Redmer et al. (2011) and Nettelmann et al. (2013) have implicitly assumed that the transition to superionic water introduces a convective barrier. It is therefore useful discuss with such type of models. We refer to them as type "B" models.

In Fig. 10, we compare the fractional layer masses and pressure and temperatures at layer boundaries for different ensembles of B-type models illustrated in Fig. 3. The blue and red points respectively show models for Neptune that we derived with our interior temperature profiles and those proposed by Redmer et al. (2011) (R11). We compare with these profiles because they are still referenced by experimentalists (Prakapenka et al. 2021). All results were obtained with the CMS method under consistent assumptions. The black and orange dots display results for Uranus with our and with R11's temperature profile. Most interesting are panels in Fig. 10 where all four distributions differ. An example is the correlation between the temperatures T_1 and T_2, temperatures at the top and bottom of the ocean layer. The four distributions vary because the planet observations and the assumed isentropes differ. For our B-type models, we predict the average values of T_1 and T_2 to be 1520 and 3000 K for Neptune and 1890 and 3370 K for Uranus. If we construct models under the same assumptions but adopt R11's temperature profiles, we obtain 1560 and 4520 K for Neptune's T_1 and T_2 and 1910 and 4510 K for Uranus. The histograms at the bottom of Fig. 10 confirm that our T_2 values for both planets are much lower than the corresponding R11 values while T_1 are fairly similar because they are not affected by our revision of the T-P profile in the ocean layer. The T_1 values for Uranus are higher simply because we predict this planet to have a thick H-He layer that encompasses 4% of the planet's mass while we predict only 1.5% for Neptune.

For T_3, the temperature between the C-N-H layer and the core, we predict an average value of 4360 and 4120 K of Uranus and Neptune. With R11's T-P profiles, we obtain much higher values of 6040 and 6100 K (also see Fig. 1). In comparison, the value of the corresponding pressure, P_3 does not change much. We predict 620 and 820 GPa for Uranus and Neptune when we adopt our P-T profile and 630 and 940 GPa for the R11 profile. Similarly our predictions for Neptune's P_2 (pressure at boundary of ocean and C-N-H layer) is lower (average of 200 GPa) than values obtained with R11's temperature profile (300 GPa). In general, Neptune's values are larger because it is a bigger planet with a bigger core. For Neptune, we predict core mass fraction of about 6.4% (1.1 Earth masses) and a central pressure of 1300 GPa while we predict a much smaller core or even no core for Uranus. The average core mass fraction in our ensembles was only 0.17% and the central pressure was 650 GPa.

The M_1-M_2 panel of Fig. 10 shows that both mass fraction are strongly anticorrelated because their densities are not very different (see Fig. 12) and one can thus move their boundary up or down

without drastically changing the gravity field. For our P-T profile we predict the ocean and C-N-H layers to encompass 57 and 39% of Uranus and each 46% of Neptune.

A number of planels in Fig. 10 show very strong correlations. For example T_1 and P_1 correlated because they are both functions of the mass of the H-He layer (M_0) and the outer adiabats are anchored at their respective 1 bar temperatures of 72 or 76 K. Similarly one finds that T_2 and P_2 are positively correlated with each other and with the mass of the ocean layer, M_1. Not surprisingly, one finds the central pressure of both planets to correlate with their core masses. One may also increase the core mass by lowering the core transition pressure, P_3, which explain why both quantities are anticorrelated.

Convection in the presence of phase transitions has been discussed in context of geophysics because different mantle minerals undergo exothermic and endothermic phase transitions in the Earth's mantle. With increasing pressure or depth, the liquid-to-superionic transition of water is similar to the exothermic transition of olivine to spinel that was analyzed by Schubert et al. (1975). When a cold slab descends, olivine, the lower-pressure phase, transforms into spinel, a higher-pressure polymorph. As its phase changes, it releases latent heat and its density decreases. Schubert et al. (1975) discussed two competing effects. First they argued that the release of latent heat would increase the local temperature, which would lower the material's density and introduce a buoyancy force that would counteract the convecting forces. Second they pointed out that a descending slab must have a temperature that is slightly lower than that of its surrounding, which means it would encounter the olivine-to-spinel transition at slightly lower pressures because the phase transition has a positive Clapeyron slope. Therefore it would transition to the higher-density spinel phase at a slightly shallower depth. There its density would be higher than that of its surrounding, which would promote the convection across the phase boundary.

Christensen (1995) analyzed the magnitude of the two effects and concluded that for Rayleigh convection in Earth's mantle, the second effect dominates over the first and that exothermic phase transitions enhance convection in general. If one adopts this picture for the convection of H_2O in the Uranus and Neptune then one is forced to represent the liquid and superionic portions of their mantles by two curves that have a same entropy. This would lead to an offset in pressure-temperature space at the melting line of superionic H_2O, which we illustrate with our models of type "C" in Figs. 1 and 3. In the gap between liquid and superionic branches, the isentrope would follow the melting line. In the planet, one would then assume there exists a *transition zone* or a mixed region where the fraction of superionic H_2O increases gradually with depth. If a cold downwelling arrived at this transition zone, it would change to superionic H_2O at slightly lower pressures, therefore become a bit denser than its surrounding, and so continue to descend. The release of latent heat would increase the temperature while the entropy remains constant because heat diffusion into the environment remains to be too slow. By similar arguments, an upwelling of hotter material would also pass through the transition zone.

In Fig. 11 we compare ensembles of models for Neptune that have constructed by assuming a single entropy value but two separate isentrope branches for the liquid and superionic phases. As expected one observes an increase in the temperatures at the water-to-CNH layer, T_2, of about 300 K (3400 instead of 3100 K) and at the CNH-core boundary, T_3 of about 500 K (4750 instead of 4250 K). Both results are much colder than values of T_2=4500 and T_3=6100 K that one would predict if one

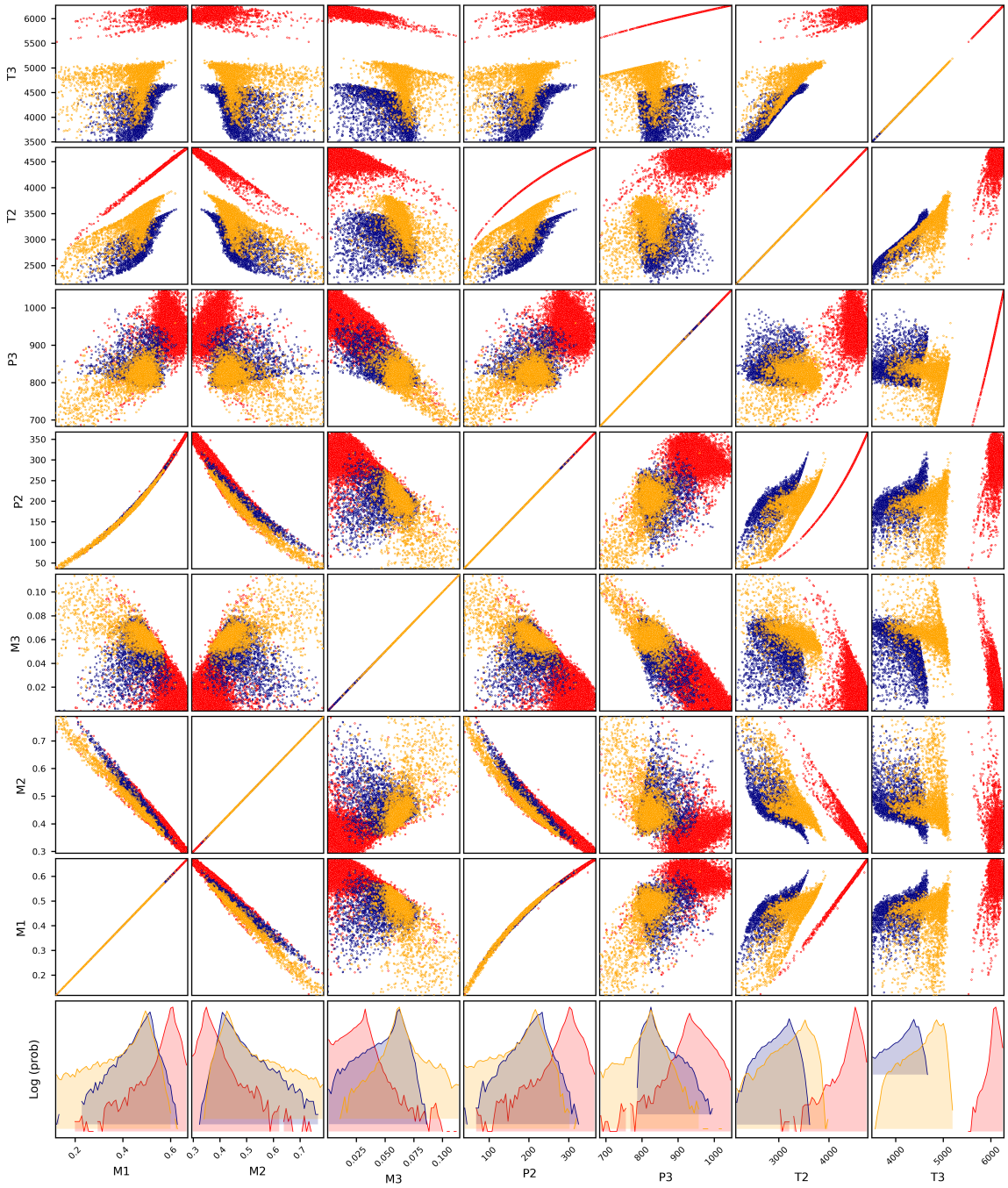

Figure 11. Like in Fig. 10, we show a posterior MCMC distribution but here we have reduced the number of variables and compare three distributions for Neptune: Red color represents models with the hotter temperature profile proposed by Redmer et al. (2011). Models of type B with a lower temperature profile that assume a convective barrier are shown in blue. The orange results represent our C type models with intermediate temperatures that assume convection occurs across the superionic-liquid boundary.

adopted the temperature profile that was proposed by Redmer et al. (2011). With this profile one predicts smaller cores (M_3), less massive CNH layers (M_2) but thicker water layers (M_1).

In Fig. 11 also shows that for B and C type models, the most likely values layer masses M_1, M_2, and M_3 and boundary pressures P_2 and P_3 are very similar but the distribution of C type models includes more massive cores that are accommodated by smaller P_2 and P_3 values. At the present time, we have no information to determine whether B and C type models more likely represent the interiors of Uranus and Neptune, so we recommend treating them as equally probable.

In Fig. 12, we show the radial profiles of density, temperature and pressure for the presentative models in Fig. 3. Because Neptune has a larger core than Uranus, the pressure and density in its center are higher. As expected, the temperature of our C-type models with a bit higher than that of our B-type models but their density and pressure profiles are rather similar. The temperature in a Neptune model by Nettelmann et al. (2013) are significantly higher than ours, which explains why they predicted a larger core for Neptune and the density in their water layer is comparable to that in our water-hydrogen layer.

4. CONCLUSIONS

We performed *ab initio* computer simulations of liquid and superionic H_2O for conditions of high pressure and temperature in the interiors of Uranus and Neptune. We derived the free energies by employing thermodynamic integration methods, which gave us a direct access to the *ab initio* entropies. This enabled us to compute isentropes and to construct models for the interiors of Uranus and Neptune. We put together two types of models assuming that convection may or may not reach across the transition between liquid and superionic water.

We propose a revision for the interior temperature profiles of Uranus and Neptune, as for both types of models we predict their deep interiors to be much colder (∼4300 or ∼4800) than earlier models by Redmer et al. (2011) and Nettelmann et al. (2013) (∼6000 K) who did not have access to entropies that were computed with *ab initio* simulations. Models by Hubbard & MacFarlane (1980), Chau et al. (2011), and by Neuenschwander et al. (2024) had predicted even higher temperatures for the interiors of Uranus and Neptune, so consequently our temperatures deviate from them even more.

Our predictions for lower temperatures in Uranus and Neptune have a number of likely consequences. They make it much more likely for diamonds to form (Ross 1981) or for the phase separation of planetary ices (Militzer 2024a) to have occurred in these planets. Future compression experiments such as these performed by Chau et al. (2011), Kraus et al. (2017), and Frost et al. (2024) may be designed to target a lower temperature range. This means there is a smaller temperature differential between the atmosphere and deep interiors, which implies that there is less energy available to drive thermal convection and to generate magnetic fields today. It also means that Uranus and Neptune have radiated more thermal energy into space since their formation, which evolution models will need to take into account when they target today's interior state that is now substantially colder than was previously predicted.

Based on results from our *ab initio* simulations, we constructed static models for the interior structure of Uranus and Neptune with the Concentric MacLaurin Spheroid method. Neptune is that predicted to have a rocky core that comprised approximately one Earth mass while Uranus is predicted to have a smaller rocky core or no core at all.

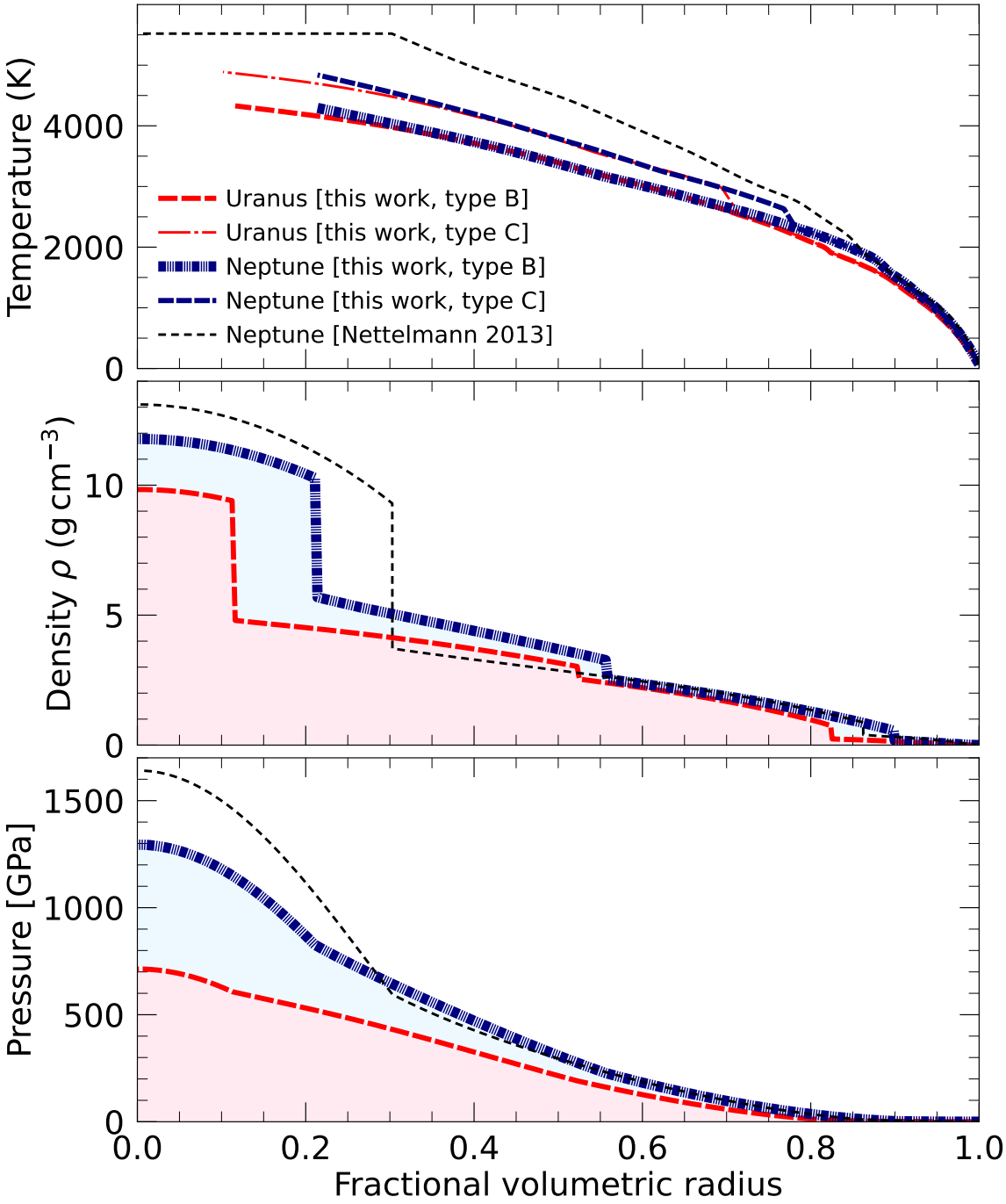

Figure 12. Radial profiles of temperature, density, and pressure from our models in Fig. 3. For comparison, we show a model by Nettelmann et al. (2013) that proposed a much hotter interior and a larger core for Neptune.

Kyla de Villa provided comments on this manuscript. This work was supported by the Department of Energy-National Nuclear Security Administration (DE-NA0004147) via the Center for Matter at Extreme Conditions and by the Juno mission of the National Aeronautics and Space Administration.

REFERENCES

Allen, M., & Tildesley, D. 1987, Computer Simulation of Liquids (New York: Oxford University Press)

Bailey, E., & Stevenson, D. J. 2021, The Planetary Science Journal, 2, 64, doi: 10.3847/PSJ/abd1e0

Bethkenhagen, M., Cebulla, D., Redmer, R., & Hamel, S. 2015, The Journal of Physical Chemistry A, 119, 10582

Cavazzoni, C., Chiarotti, G. L., Scandolo, S., et al. 1999, Nature, 283, 44

Chau, R., Hamel, S., & Nellis, W. J. 2011, Nature Communications, 2, 203, doi: 10.1038/ncomms1198

Christensen, U. 1995, Annual Review Of Earth And Planetary Sciences, Volume 23, pp. 65-88., 23, 65

de Villa, K., González-Cataldo, F., & Militzer, B. 2023, Nature Communications, 14, 7580

—. 2025, Contributions to Plasma Physics, e70015

de Wijs, G. A., Kresse, G., & Gillan, M. J. 1998, Phys. Rev. B, 57, 8223

French, M., Mattsson, T. R., Nettelmann, N., & Redmer, R. 2009, Phys. Rev. B, 79, 054107

French, R. G., Hedman, M. M., Nicholson, P. D., Longaretti, P.-Y., & McGhee-French, C. A. 2024, Icarus, 411, 115957

Frost, M., McWilliams, R. S., Bykova, E., et al. 2024, Nature astronomy, 8, 174

González-Cataldo, F., Wilson, H. F., & Militzer, B. 2014, The Astrophysical Journal, 787, 79

Guillot, T., Stevenson, D. J., Hubbard, W. B., & Saumon, D. 2004, The interior of Jupiter, ed. D. T. E. . M. W. B. Bagenal, F., 35–57

Helled, R., & Bodenheimer, P. 2014, The Astrophysical Journal, 789, 69, doi: 10.1088/0004-637X/789/1/69

Helled, R., Nettelmann, N., & Guillot, T. 2020, Space Science Reviews, 216, 38, doi: 10.1007/s11214-020-00660-3

Hubbard, W. B. 1984, Planetary Interiors (Tucson, AZ: University of Arizona Press)

—. 2013, The Astrophysical Journal, 768, 43

Hubbard, W. B., & MacFarlane, J. J. 1980, Journal of Geophysical Research: Solid Earth, 85, 225

Hubbard, W. B., & Militzer, B. 2016, Astrophys. J., 820, 80

Huber, K. 2013, Molecular spectra and molecular structure: IV. Constants of diatomic molecules (Springer Science & Business Media)

Izvekov, S., Parrinello, M., Burnham, C. J., & Voth, G. A. 2003, J. Chem. Phys., 120, 10896

Kraus, D., Vorberger, J., Pak, A., et al. 2017, Nature Astronomy, 1, 606

Kresse, G., & Furthmüller, J. 1996, Phys. Rev. B, 54, 11169

Kresse, G., & Joubert, D. 1999, Phys. Rev. B, 59, 1758, doi: 10.1103/PhysRevB.59.1758

Leconte, J., & Chabrier, G. 2012, Astronomy & Astrophysics, 540, A20

Lin, Z., Seager, S., & Weiss, B. P. 2025, The Planetary Science Journal, 6, 27

Matusalem, F., Santos Rego, J., & de Koning, M. 2022, Proceedings of the National Academy of Sciences, 119, e2203397119

Militzer, B. 2013, Physical Review B, 87, 014202

—. 2016, High Energy Density Physics, 21, 8

—. 2023a, The Astrophysical Journal, 953, 111, doi: 10.3847/1538-4357/ace1f1

—. 2023b, Quadratic Monte Carlo, 03-08-23, Zenodo, doi: 10.5281/zenodo.8038144

—. 2024a, Proceedings of the National Academy of Sciences, 121, e2403981121

—. 2024b, Quadratic Monte Carlo 2024, Zenodo, doi: 10.5281/zenodo.13961175

—. 2025a, "Ideal Mixture of Hydrogen and Helium", Zenodo, DOI 10.5281/zenodo.15848727, Zenodo, doi: 10.5281/zenodo.15848727

—. 2025b, Computer Physics Communications, 307, 109424

—. 2025c, "H2O Equation of State and Interior Models of Uranus and Neptune", Zenodo, DOI 10.5281/zenodo.15848859, Zenodo, doi: 10.5281/zenodo.15848859

Militzer, B., & Hubbard, W. B. 2007, AIP Conf. Proc., 955, 1395

—. 2013, Astrophys. J., 774, 148

—. 2024, Icarus, 411, 115955, doi: https://doi.org/10.1016/j.icarus.2024.115955

Militzer, B., Hubbard, W. H., Vorberger, J., Tamblyn, I., & Bonev, S. A. 2008, Astrophys. J. Lett., 688, L45

Militzer, B., Wahl, S., & Hubbard, W. B. 2019, The Astrophysical Journal, 879, 78, doi: 10.3847/1538-4357/ab23f0

Militzer, B., & Zhang, S. 2018, AIP Conference Proceedings, 1979, 050012

Militzer, B., Hubbard, W. B., Wahl, S., et al. 2022, Planet. Sci. J., 3, 185

Millot, M., Coppari, F., Rygg, J. R., et al. 2019, Nature, 569, 251

Morales, M. A., Schwegler, E., Ceperley, D., et al. 2009, Proceedings of the National Academy of Sciences, 106, 1324

Movshovitz, N., & Fortney, J. J. 2022, The Planetary Science Journal, 3, 88

NASA. 2021. https://science.nasa.gov/wp-content/uploads/2023/10/uranus-orbiter-and-probe.pdf

Nettelmann, N., Helled, R., Fortney, J., & Redmer, R. 2013, Planetary and Space Science, 77, 143, doi: https://doi.org/10.1016/j.pss.2012.06.019

Neuenschwander, B. A., Müller, S., & Helled, R. 2024, Astron. and Astrophys., in press, arXiv preprint arXiv:2401.11769, in press

NIST. 2025. http://webbook.nist.gov/cgi/cbook.cgi?ID=C1333740&Units=SI&Mask=1000#Diatomic

Nosé, S. 1984, Journal of Chemical Physics, 81, 511

Perdew, J. P., Burke, K., & Ernzerhof, M. 1996, Phys. Rev. Lett., 77, 3865

Podolak, M., Weizman, A., & Marley, M. 1995, Planetary and Space Science, 43, 1517, doi: https://doi.org/10.1016/0032-0633(95)00061-5

Prakapenka, V. B., Holtgrewe, N., Lobanov, S. S., & Goncharov, A. F. 2021, Nature Physics, 17, 1233

Redmer, R., Mattsson, T. R., Nettelmann, N., & French, M. 2011, Icarus, 211, 798, doi: https://doi.org/10.1016/j.icarus.2010.08.008

Ross, M. 1981, Nature, 292, 435

Ruzmaikin, A., & Starchenko, S. 1991, Icarus, 93, 82

Saumon, D., & Chabrier, G. 1991, Physical Review A, 44, 5122

—. 1992, Phys. Rev. A, 46, 2084

Schubert, G., Yuen, D. A., & Turcotte, D. L. 1975, Geophysical Journal International, 42, 705

Soderlund, K., Heimpel, M., King, E., & Aurnou, J. 2013, Icarus, 224, 97

Soderlund, K., & Stanley, S. 2020, Philosophical Transactions of the Royal Society A, 378, 20190479

Soubiran, F., & Militzer, B. 2015, The Astrophysical Journal, 806, 228

Stanley, S., & Bloxham, J. 2004, Nature, 428, 151, doi: 10.1038/nature02376

—. 2006, Icarus, 184, 556

Stixrude, L., Baroni, S., & Grasselli, F. 2021, The Planetary Science Journal, 2, 222

Sun, J., Clark, B. K., Torquato, S., & Car, R. 2015, Nature communications, 6, 8156

Wahl, S. M., & Militzer, B. 2015, Earth and Planetary Science Letters, 410, 25

Wahl, S. M., Wilson, H. F., & Militzer, B. 2013, The Astrophysical Journal, 773, 95

Wilson, H. F., & Militzer, B. 2012a, Astrophys. J., 745, 54

—. 2012b, Phys. Rev. Lett., 108, 111101

Wilson, H. F., Wong, M. L., & Militzer, B. 2013, Physical review letters, 110, 151102